

# Development of a discontinuous Galerkin ionosphere-plasmasphere model

Houjun Wang<sup>1</sup>

<sup>1</sup>CIRES-University of Colorado

November 22, 2022

## Abstract

The objective of this study is to explore the application of high-order numerical methods in ionosphere-plasmasphere modeling. Specifically, the nodal discontinuous Galerkin (DG) method is chosen to solve the multifluid dynamical equations along the magnetic field lines. A general curvilinear magnetic field-line-following coordinate system is also used in the model. Numerical simulations with different combinations of number of elements (K) and polynomial orders (N) show the *converging* results, indicating the robustness of the algorithms and implementation. The model also captures the dawn terminator effect very well in the He<sup>+</sup> field.

1                    **Development of a discontinuous Galerkin**  
2                    **ionosphere-plasmasphere model**

3                    **Houjun Wang**

4                    CIRES, University of Colorado at Boulder, Colorado, USA

5                    **Key Points:**

- 6                    • The high-order discontinuous Galerkin (DG) method is used to solve the multi-  
7                    fluid plasma dynamical equations along the magnetic field line  
8                    • Converging results of simulations with different element size and polynomial or-  
9                    der indicate robustness of algorithms and implementation  
10                   • The model algorithms also capture the dawn terminator effect very well in the He<sup>+</sup>  
11                   density field

## Abstract

The objective of this study is to explore the application of high-order numerical methods in ionosphere-plasmasphere modeling. Specifically, the nodal discontinuous Galerkin (DG) method is chosen to solve the multifluid dynamical equations along the magnetic field lines. A general curvilinear magnetic field-line-following coordinate system is also used in the model. Numerical simulations with different combinations of number of elements (K) and polynomial orders (N) show the *converging* results, indicating the robustness of the algorithms and implementation. The model also captures the dawn terminator effect very well in the  $\text{He}^+$  field.

## 1 Introduction

The Earth's ionosphere and plasmasphere is a multi-fluid system involving complex physical-chemical and electrodynamic processes that span many orders of magnitude changes. This complexity presents a great challenge to numerical methods for accurate simulation of the ionosphere-plasmasphere system.

Many ionospheric models use the finite-difference methods of at most second-order accuracy with the central difference scheme (e.g., R. W. Schunk, 1996). Some ionospheric models use only approximated equations, e.g., the time-dependent inertial terms are ignored in the momentum equation (e.g., Bailey & Balan, 1996). A good assessment on some of the ionospheric models used at that time was given by Huba et al. (2000). The SAMI2 model (Huba et al., 2000) uses the upwind differencing scheme, or the donor cell method, which is conservative but highly diffusive and only first-order accurate. Some newer ionospheric models (e.g., Zettergren & Semeter, 2012) are also using the low-order numerical methods. However, it should be noted that the SAMI3 model uses the high-order interpolation scheme in conjunction with partial donor cell method (Hain, 1987; Huba, 2003). The high-order schemes are used to avoid the excessive numerical diffusion of the low-order methods and to allow steeper density gradients to develop in irregularity simulation (Huba & Liu, 2020).

The advance of high-order numerical methods, such as the spectral element (SE) or discontinuous Galerkin (DG) methods, provides a great opportunity to meet the challenge in modeling the complex multi-scale processes of the ionosphere-plasmasphere system. As defined in Gustafsson (2008), the high-order methods refer to those methods whose order of accuracy  $p \geq 3$ . Here the order of accuracy  $p$  is defined in such a way that the truncation error is proportional to  $h^p$ , with  $h$  as the discretization step size. The high-order methods are advantageous for solving the wave propagation problems and/or when more accurate solutions of problems are required (e.g, Gustafsson, 2008). High-order spectral methods also have significantly lower phase errors compared to the finite-difference methods (e.g., Canuto et al., 2006). As discussed in Hesthaven (2018), the motivation for development of high-order accurate schemes is “to do more with less, i.e., to develop schemes that are more accurate than first order accurate schemes without substantially increasing the computational cost.”

The main advantages of the DG methods over classical finite volume and finite difference methods are (Cockburn et al., 2000):

- Arbitrarily high formal order of accuracy can be obtained by suitably choosing the degree of the approximating polynomials
- Highly parallelizable
- Suitable to handle complicated geometries and simple in treating boundary conditions
- Easy in handling adaptivity

In this study, we explore the applications of the DG methods in ionosphere-plasmasphere modeling. We develop a new ionosphere-plasmasphere model using the DG methods to solve the dynamics and diffusion equations along the geomagnetic field lines. The splitting method is used to solve the ionosphere-plasmasphere model equations sequentially. First, the Euler equations with gravity along the field lines are solved using the DG method for spatial discretization and the strong stability preserving Runge-Kutta method (SSP-RK) for time integration with adaptive time stepping. Then, the thermal diffusion equations for ions and electrons along the field lines are solved using the DG method and Crank-Nicolson (CN) implicit time stepping. Various physical-chemical forcing, including photoionization, chemical productions and losses, collisions, and heating and cooling terms, are then added using a positive-definite ordinary differential equation (ODE) solver. The perpendicular ExB transport is done using a simple semi-Lagrangian (SL) transport scheme, with specified ExB drift velocity mimic empirical ExB drift model.

In addition to the DG methods used in the model, several other new features are introduced in the model. The *ragged array* with variable array length/size along the field lines is used in the model. This approach is very suitable to the ionosphere-plasmasphere modeling considering the varying length of magnetic field lines. It does not involve complicated derived data types (DDT) and saves both computing memory and disk space storage. Another feature is that the native MPI-IO is used for model input and output. This approach is simple and efficient, which works very well with the simple decomposition that divides the model domain into meridional sections/slabs along the geomagnetic longitudes for the MPI tasks. And finally, a new general curvilinear field-line-following coordinate system (Wang, 2021) is also used in the model.

This paper is organized as follows. In the next section, we describe various aspects of the DG model: the nodal DG method for the field-aligned dynamics and diffusion, the physical-chemical forcing ODE solver, the perpendicular ExB transport, and some aspects of the model code. In section 3, we present results of model simulations using different combinations of number of elements (K) and polynomial orders (N), showing the converging results of the total electron content (TEC) and model's ability to capture the terminator effect. And a summary is given in section 4. Some mathematical details related to the DG methods, such as limiter and filter, and computation of physical forcing terms are given in the Appendix.

## 2 The discontinuous Galerkin (DG) ionosphere-plasmasphere model

### 2.1 The model equations along the field line and overview of the model

The ionosphere and plasmasphere are modeled as a multi-fluid system. In the general curvilinear magnetic field-line-following coordinate system  $(\mu, \chi, \phi) \Rightarrow (\mu_m, \chi_m, \phi_m)$  (Wang, 2021), the one-dimensional Euler equations with gravity can be written as

$$\frac{\partial \rho_i}{\partial t} + \frac{1}{h_\mu h_\chi h_\phi} \frac{\partial}{\partial \mu} [h_\chi h_\phi (\rho_i u_i)] = 0, \quad (1a)$$

$$\frac{\partial \rho_i u_i}{\partial t} + \frac{1}{h_\mu h_\chi h_\phi} \frac{\partial}{\partial \mu} [h_\chi h_\phi (p_i + \rho_i u_i^2)] = -\rho_i g_{\parallel}, \quad (1b)$$

$$\frac{\partial E_i}{\partial t} + \frac{1}{h_\mu h_\chi h_\phi} \frac{\partial}{\partial \mu} [h_\chi h_\phi (E_i + p_i) u_i] = -\rho_i u_i g_{\parallel}, \quad (1c)$$

where  $\rho_i$  is density,  $\rho_i u_i$  is the momentum,  $E_i$  is the energy (internal and kinetic) per unit volume, with the subscript  $i$  denoting the different ion species;  $h_\mu, h_\chi, h_\phi$  are the scale factors; and  $g_{\parallel}$  is gravity parallel to the field line. The pressure is related to the energy through the ideal gas law as

$$p_i = (\gamma_i - 1) \left( E_i - \frac{1}{2} \rho_i u_i^2 \right), \quad c_i = \sqrt{\frac{\gamma_i P_i}{\rho_i}},$$

106 where  $c_i$  is the local speed of sound and  $\gamma_i$  is the specific heat ratio. The advantage of  
 107 using the set of equations in this conservative form is shown by Giraldo & Restelli (2008).  
 108 Using the spectral element (SE) and discontinuous Galerkin (DG) methods, they demon-  
 109 strated that numerical solutions are less dissipative when the equation set is written in  
 110 this form than in other forms discussed in their paper.

111 The set of equations of (1) excludes the diffusion and physical-chemical forcing terms,  
 112 which will be described in section 2.3 and 2.4, respectively. The perpendicular ExB drift  
 113 is discussed in section 2.5

114 Ideally, various physical-chemical source terms should be added to the dynamical  
 115 solver and treated seamlessly together in just one setting. Currently, we split the com-  
 116 putation into dynamics/advection, diffusion and physical-chemical forcing steps. As will  
 117 be discussed shortly, the dynamics/advection step is solved *explicitly* using the DG method  
 118 for spatial discretization and the strong stability preserving Runge-Kutta method (SSP-  
 119 RK) for time integration; the diffusion step is solved *implicitly* using the DG method for  
 120 spatial discretization and the Crank-Nicolson (CN) scheme for time integration; and the  
 121 physical-chemical forcing part is solved using an unconditionally stable positive-definite  
 122 scheme. Using the so-called Strang operator splitting (Strang, 1968), the advection-diffusion-  
 123 chemical (ADC) operators are treated sequentially as follows (e.g, Fazio & Jannelli (2010)):

$$124 \quad \frac{\partial q}{\partial t} = \mathcal{A}(\delta t/2)\mathcal{D}(\delta t/2)\mathcal{C}(\delta t)\mathcal{D}(\delta t/2)\mathcal{A}(\delta t/2)q,$$

125 which results in a second-order splitting error. However, this can be expensive. To save  
 126 time, we can simply use

$$127 \quad \frac{\partial q}{\partial t} = \mathcal{C}(\delta t)\mathcal{D}(\delta t)\mathcal{A}(\delta t)q,$$

128 which is used in the simulations discussed in this paper.

## 129 2.2 The nodal discontinuous Galerkin methods for field-aligned dynam- 130 ics

131 We rewrite the set of equations (1) in the vector form as

$$132 \quad \frac{\partial \mathbf{q}}{\partial t} + \frac{\partial \mathbf{F}}{\partial x} = \mathbf{G}, \quad (2)$$

133 where

$$134 \quad \mathbf{q} = \begin{bmatrix} \rho_i \\ \rho_i u_i \\ E_i \end{bmatrix}, \quad \mathbf{F} = \begin{bmatrix} h_\chi h_\phi (\rho_i u_i) \\ h_\chi h_\phi (p_i + \rho_i u_i^2) \\ h_\chi h_\phi (E_i + p_i) u_i \end{bmatrix}, \quad \mathbf{G} = \begin{bmatrix} 0 \\ -\rho_i g_\parallel \\ -\rho_i u_i g_\parallel \end{bmatrix}.$$

135 The equation system is solved using the nodal discontinuous Galerkin (DG) methods (e.g.,  
 136 Hesthaven & Warburton, 2008).

137 Approximate the 1D domain  $\Omega = [x_L, x_R]$  by  $K$  non-overlapping elements  $\mathbf{D}^k =$   
 138  $[x_l^k, x_r^k]$ . On each element, we introduce  $N_p$  local grid points,  $x_i^k \in \mathbf{D}^k$ , usually the Legendre-  
 139 Gauss-Lobatto (LGL) quadrature points (e.g., Deville et al., 2002; Canuto et al., 2006).  
 140 In the nodal representation, we express the local solution and the local flux as a poly-  
 141 nomial of order  $N = N_p - 1$ , through the associated interpolating Lagrange polynomial,  
 142  $\ell_i^k(x)$ , as follows:

$$143 \quad \mathbf{q}_h^k(x, t) = \sum_{i=1}^{N_p} \mathbf{q}_h^k(x_i^k, t) \ell_i^k(x), \quad \mathbf{F}_h^k(\mathbf{q}_h^k(x, t)) = \sum_{i=1}^{N_p} \mathbf{F}_h^k(x_i^k, t) \ell_i^k(x),$$

144 and similarly for the right-hand side term. The nodal values  $\mathbf{q}_h^k(x_i^k, t)$  are the unknowns.  
 145 Then on each element, we require that the residual is orthogonal to the test function,  
 146 which is the same as the basis function for the Galerkin method,

$$147 \quad \int_{\mathbf{D}^k} \left( \frac{\partial \mathbf{q}_h^k}{\partial t} + \frac{\partial \mathbf{F}_h^k}{\partial x} - \mathbf{G}_h^k \right) \ell_j^k(x) dx = 0.$$

148 Interpolation by parts yields

$$149 \int_{\mathcal{D}^k} \left( \frac{\partial \mathbf{q}_h^k}{\partial t} \ell_j^k - \mathbf{F}_h^k \frac{d\ell_j^k}{dx} - \mathbf{G}_h^k \ell_j^k \right) dx = -[\mathbf{F}_h^k \ell_j^k]_{x_l^k}^{x_r^k}.$$

150 The main purpose of the right-hand side is to connect the neighboring elements. A nu-  
 151 merical flux  $\mathbf{F}^*$  is introduced as a unique value to be used at the element interface. The  
 152 numerical flux is obtained by combining information from neighboring elements and should  
 153 appropriately reflect the underlying dynamics of the problem.

154 With this we obtain the DG scheme for the conservation laws in *weak form* as

$$155 \int_{\mathcal{D}^k} \left( \frac{\partial \mathbf{q}_h^k}{\partial t} \ell_j^k - \mathbf{F}_h^k \frac{d\ell_j^k}{dx} - \mathbf{G}_h^k \ell_j^k \right) dx = -[\mathbf{F}^* \ell_j^k]_{x_l^k}^{x_r^k}.$$

156 Integration by parts once more, we get the DG scheme in *strong form* as

$$157 \int_{\mathcal{D}^k} \left( \frac{\partial \mathbf{q}_h^k}{\partial t} + \frac{\partial \mathbf{F}_h^k}{\partial x} - \mathbf{G}_h^k \right) \ell_j^k(x) dx = [(\mathbf{F}_h^k - \mathbf{F}^*) \ell_j^k]_{x_l^k}^{x_r^k}.$$

158 In matrix form this can be written as

$$159 \mathcal{M}^k \frac{d}{dt} \mathbf{q}_h^k + \mathcal{S} \mathbf{F}_h^k - \mathcal{M}^k \mathbf{G}_h^k = [\ell^k(x)(\mathbf{F}_h^k - \mathbf{F}^*)]_{x_l^k}^{x_r^k},$$

160 where we have introduced the local mass and stiffness matrices:

$$161 \mathcal{M}_{ij}^k = \int_{\mathcal{D}^k} \ell_i^k(x) \ell_j^k(x) dx, \quad \mathcal{S}_{ij}^k = \int_{\mathcal{D}^k} \ell_i^k(x) \frac{d\ell_j^k}{dx} dx.$$

162 For the numerical flux  $\mathbf{F}^*$ , we use the monotone Lax-Friedrichs flux:

$$163 \mathbf{F}^*(\mathbf{q}_h^-, \mathbf{q}_h^+) = \{ \{ \mathbf{F}_h(\mathbf{q}_h) \} \} + \frac{C}{2} \llbracket \mathbf{q}_h \rrbracket,$$

164 where  $C = \max |\mathbf{F}_q|$  is an upper bound on the (local) wave speed. The average  $\{ \{ \cdot \} \}$   
 165 and the jump  $\llbracket \cdot \rrbracket$  (along a cell interface with normal  $\mathbf{n}$ ) are defined as

$$166 \{ \{ u \} \} = (u^- + u^+)/2, \quad \llbracket u \rrbracket = \mathbf{n}^- u^- + \mathbf{n}^+ u^+,$$

167 where the superscripts “-” and “+” refer to the interior and exterior values at the cell  
 168 interface, respectively.

169 For time integration we use the strong stability preserving Runge-Kutta method  
 170 (SSP-RK) (e.g., Gottlieb et al., 2001; Hesthaven & Warburton, 2008), such that no in-  
 171 stability would be introduced by time integration if the Courant-Friedrichs-Lewy (CFL)  
 172 criteria (Courant et al., 1967) are satisfied. The semidiscrete equation

$$173 \frac{du_h}{dt} = \mathcal{L}_h(u_h, t)$$

174 is solved using the optimal third-order three-stage SSP-RK scheme as follows

$$175 v^{(1)} = u_h^n + \Delta t \mathcal{L}_h(u_h^n, t^n),$$

$$176 v^{(2)} = \frac{1}{4} \left( 3u_h^n + v^{(1)} + \Delta t \mathcal{L}_h(v^{(1)}, t^n + \Delta t) \right),$$

$$177 u_h^{n+1} = v^{(3)} = \frac{1}{3} \left( u_h^n + 2v^{(2)} + 2\Delta t \mathcal{L}_h \left( v^{(2)}, t^n + \frac{1}{2}\Delta t \right) \right).$$

179 The slope limiter is applied on the characteristic variables after each time step, see Ap-  
 180 pendix A for details.

### 2.3 Discontinuous Galerkin for diffusion

The one-dimensional thermal diffusion equation for ions and electrons along the magnetic field line can be written, with the scale factors, as

$$\frac{\partial T}{\partial t} = \frac{2}{3} \frac{1}{nk_B} \frac{1}{h_\chi h_\phi} \frac{\partial}{\partial \mu} \left( h_\chi h_\phi \kappa \frac{\partial T}{h_\mu \partial \mu} \right), \quad (3)$$

where  $T = T_{i,e}$  is the temperature,  $n = n_{i,e}$  is the number density and  $\kappa = \kappa_{i,e}$  is the diffusion coefficient, with the subscripts  $i$  and  $e$  denoting ion and electron, respectively; and  $k_B$  is the Boltzmann constant. Expressions for computing thermal conductivities are given in Appendix B1. Write the diffusion equation (3) in the form

$$\frac{\partial T}{\partial t} = b \frac{\partial}{\partial x} \left( a \frac{\partial T}{\partial x} \right),$$

and then rewrite it as a system of the first-order equations

$$\frac{\partial T}{\partial t} = b \frac{\partial}{\partial x} (\sqrt{a}q), \quad q = \sqrt{a} \frac{\partial T}{\partial x}, \quad (4)$$

which is what to be solved using the DG methods.

The DG discretization of the system of equations (4) can be written in matrix form as

$$\mathcal{M}^k \frac{d\mathbf{T}_h^k}{dt} = \mathcal{B}^k \mathcal{S}^k \mathcal{A}^k \mathbf{q}_h^k - [\ell^k(x)((b\sqrt{a}q_h^k) - (b\sqrt{a}q_h^k)^*)]_{x_i^k}^{x_r^k}, \quad (5a)$$

$$\mathcal{M}^k \mathbf{q}_h^k = \mathcal{A}^k \mathcal{S}^k \mathbf{T}_h^k - [\ell^k(x)((\sqrt{a}T_h^k) - (\sqrt{a}T_h^k)^*)]_{x_i^k}^{x_r^k}, \quad (5b)$$

where  $\mathcal{A}_{ii}^k = \sqrt{a(x_i^k)}$  and  $\mathcal{B}_{ii}^k = b(x_i^k)$ . The numerical flux are chosen as follows:

$$(b\sqrt{a}q_h^k)^* = \{\{b\sqrt{a}q_h^k\}\} - \tau \llbracket abu_h^k \rrbracket, \quad (\sqrt{a}T_h^k)^* = \{\{\sqrt{a}T_h^k\}\},$$

with an interior penalty  $\tau$  term to disallow large jumps at the element interface and to stabilize the solution. The penalty parameter, or the stabilization parameter,  $\tau$ , is chosen such that (Shahbazi, 2005; Hesthaven & Warburton, 2008)

$$\tau \geq c_\tau N_p^2/h, \quad c_\tau \geq 1/2,$$

where  $h$  is the element size. We use  $c_\tau = 3/2$  in all simulations discussed in this paper.

For the time integration of the diffusion equation, we write the diffusion equation after the DG discretization (5) in the semidiscrete form as

$$\frac{dT_h}{dt} = \mathbb{H}T_h,$$

and then use the second-order implicit Crank-Nicolson (CN) scheme for time discretization as

$$\frac{T_h^{n+1} - T_h^n}{\Delta t} = \frac{1}{2}(\mathbb{H}T_h^{n+1} + \mathbb{H}T_h^n),$$

or

$$\left( \mathbb{I} - \frac{1}{2} \Delta t \mathbb{H} \right) T_h^{n+1} = \left( \mathbb{I} + \frac{1}{2} \Delta t \mathbb{H} \right) T_h^n,$$

which is to be solved using the LAPACK's linear solver 'dgbsv' for the system of linear equations with the general banded matrix (Anderson et al., 1999). The exponential filter is then used. It should be noted that the DG for diffusion with large varying diffusivity is indeed a challenging problem (e.g., Proft & Rivière, 2009). The combination of the DG discretization with the interior penalty term and filtering seems to work well.

## 2.4 Adding the physical-chemical forcing terms

Various physical-chemical source terms appear in the equations of the ionosphere-plasmasphere model. As discussed above, we use the operator splitting scheme in this study. The physical-chemical source terms are added to the model by solving the following set of ordinary differential equations (ODEs):

$$\frac{dn_i}{dt} = P_i - n_i L_i, \quad (6a)$$

$$\frac{du_i}{dt} = -\nu_{in}(u_i - u_n) - \sum_j \nu_{ij}(u_i - u_j), \quad (6b)$$

$$\frac{dT_i}{dt} = Q_{in} + Q_{ii} + Q_{ie}, \quad (6c)$$

$$\frac{dT_e}{dt} = Q_{en} + Q_{ei} + Q_{phe}, \quad (6d)$$

where  $P_i$  and  $L_i$  are the ion production and ion loss terms;  $\nu_{in}$  and  $\nu_{ij}$  are ion-neutral and ion-ion collision frequencies; and  $Q_{phe}$  is the photoelectron heating rate. Other collisional heating terms are given by:

$$Q_{in} = \frac{2}{3} \sum_q \frac{m_i m_q}{(m_i + m_q)^2} \nu_{iq} \left[ 3(T_q - T_i) + \frac{m_q}{k_B} (u_q - u_i)^2 \right], \quad (7a)$$

$$Q_{ii} = \frac{2}{3} \sum_j \frac{3.3 \times 10^{-4} n_j}{A_i A_j (T_i/A_i + T_j/A_j)^{3/2}} (T_j - T_i), \quad (7b)$$

$$Q_{ie} = \frac{2}{3} \frac{7.7 \times 10^{-6} n_e}{A_i T_e^{3/2}} (T_e - T_i), \quad (7c)$$

$$Q_{en} = \frac{2}{3} \sum_q \frac{m_e m_q}{(m_e + m_q)^2} \nu_{eq} [3(T_q - T_e)], \quad (7d)$$

$$Q_{ei} = \frac{2}{3} \sum_j \frac{7.7 \times 10^{-6} n_j}{A_j T_e^{3/2}} (T_j - T_e), \quad (7e)$$

where  $q$  denotes summation over neutrals and  $j$  summation over ions. The Appendix B gives more details on computation of collision frequency and heating rate and a brief description of a simple photoelectron heating model, but see Huba et al. (2000) for the description of photoionization and chemistry model. The computation of the physical-chemical forcing terms are based on SAMI2 open source code modified for the current model.

The set of ODEs for the physical-chemical forcing can be written in the form of production-destruction equation as follows:

$$\frac{dc_i}{dt} = P_i(\mathbf{c}) - D_i(\mathbf{c}),$$

where  $P_i(\mathbf{c}) \geq 0$  and  $D_i(\mathbf{c}) \geq 0$  represent the production and destruction rates of the  $i$ th constituent, respectively. The set of production-destruction equations is solved with the Patankar-Euler integration scheme (Burchard et al., 2003) as

$$c_i^{n+1} = c_i^n + \Delta t \left( P_i(\mathbf{c}^n) - D_i(\mathbf{c}^n) \frac{c_i^{n+1}}{c_i^n} \right),$$

using the so-called Patankar trick (Patankar, 1980). This is a (unconditionally) positive scheme, i.e.,  $c_i^{n+1} > 0$  for any  $c_i^n > 0$  with any time step size  $\Delta t \geq 0$ .

## 2.5 The perpendicular transport: ExB drift

Simple vertical and zonal ExB drift velocity profiles that mimic the empirical ExB model (e.g., Scherliess & Fejer, 1999; Fejer et al., 2005) are used in this study, similar

254 to what is used in the SAMI2 model. The vertical and zonal ExB drift velocities at the  
 255 magnetic equator are given by

$$256 \quad v_{\text{exb}} = v_0 \sin(2\pi(h_{\text{lt}} - 6)/24) + v_{\text{pre}} \exp[-(h_{\text{lt}} - 19)/\delta_{\text{pre}}]^2], \quad (8)$$

257 where  $v_0 = 25$ ,  $v_{\text{pre}} = 50$  for vertical drift and  $v_0 = -40$ ,  $v_{\text{pre}} = 120$  for zonal drift,  
 258  $\delta_{\text{pre}} = 2$ , with the subscript ‘pre’ denoting the ‘pre-reversal enhancement’. The sim-  
 259 ple ExB drift velocity model gives more flexibilities in model development and testing  
 260 in terms of adjusting the model parameters.

261 The algorithm for the ExB drift is implemented in the sense that plasma along each  
 262 flux tube moves as a whole, taking into account of the effect of flux tube volume change  
 263 on plasma density and adiabatic effect on temperature. Currently the low-order, non-  
 264 conservative semi-Lagrangian (SL) scheme is used in the model. In the future, conser-  
 265 vative high-order transport schemes, such as the semi-Lagrangian discontinuous Galerkin  
 266 (SLDG) scheme (e.g., Cai et al., 2017), will be implemented.

## 267 2.6 Some aspects of the model code

268 We should point out a few features of the model’s source code. The model uses stan-  
 269 dard Fortran 90 or later features, without sophisticated data structure or derived data  
 270 types (DDT). However, the *ragged array* with variable length is used. This is found to  
 271 be very useful in representing the data of variable length along the geomagnetic field lines,  
 272 which can save data storage space and/or runtime memories. It can also improve over-  
 273 all model efficiency. Here is an example on using the ragged array:

```

274 ! define an allocatable data type for variable length
275 type vc1d
276     real(dp), allocatable :: vc1d(:)
277 end type vc1d
278
279 ! use the data type to define a ragged array
280 type(vc1d), dimension(:,,:), allocatable :: b
281
282 ! allocate the ragged array with variable length,
283 !           i.e., klm(l,m) depending on (l,m)
284 allocate ( b(nlp,nmp) )
285 do m = 1, nmp
286 do l = 1, nlp
287 allocate ( b(l,m)%vc1d( klm(l,m) ) )
288 enddo
289 enddo

```

290 Another feature of the model is that MPI-IO (Gropp et al., 2014) is used for model  
 291 input and output, which improves model I/O efficiency. This approach appears to be sim-  
 292 pler than using other parallel I/O libraries, such as HDF-5 ([https://en.wikipedia.org/  
 293 wiki/Hierarchical\\_Data\\_Format](https://en.wikipedia.org/wiki/Hierarchical_Data_Format)) or PnetCDF ([https://parallel-netcdf.github  
 294 .io/](https://parallel-netcdf.github.io/)).

## 295 3 Numerical simulations and results

296 We demonstrate the model with three-dimensional simulations using different com-  
 297 binations of number of elements (K) and polynomial orders (N). The first set of simu-  
 298 lations uses the same number of elements, but varies the polynomial orders (from N =  
 299 2 to 4). The second set of simulations varies both K and N such that the overall reso-  
 300 lutions are similar between the simulations.

**Table 1.** The total number of elements.

	K101	K135	K201
Number of elements	1 147 886	1 545 019	2 315 954

### 3.1 Model configurations

The number of grid points in the zonal and meridional direction, or the magnetic longitudes and latitudes, is the same for all simulations. We use 225 grid points between magnetic co-latitudes  $45^\circ$  and  $82^\circ$ , and 90 grid points in magnetic longitudes. The grid resolution along the flux tube is determined by the number of points along the *outermost* flux tube between the two foot points where they cross the Earth's surface. Note that the model uses only nodal points whose altitudes are higher than 90 km; see Wang (2021) for details on grid generation and metric coefficients computation.

In this study, three set of model resolutions along the flux tube are used. The numbers of nodal points along the outermost flux tube between the two foot points are 101, 135 and 201, which will be denoted by K101, K135 and K201, respectively, in the following discussion. The corresponding total number of elements for each K-resolution is shown in Table 1,

To demonstrate the implementation of the algorithms described in section 2, we examine simulation results using three different polynomial orders,  $N = 2, 3, 4$ , which have the corresponding formal order of accuracy of  $N_p = N + 1 = 3, 4, 5$ . In the first set of runs, the number of elements along the flux tubes is kept the same, K101. In the second set of runs, the number of elements and polynomial order are chosen such that the overall resolutions are about the same along the flux tubes. We have used combinations of K201/N2, K135/N3 and K101/N4 in this set of runs; see Table 2.

The model solves for the ion density, temperature, and the field-aligned velocity and electron temperature. Seven ion species ( $H^+$ ,  $He^+$ ,  $O^+$ ,  $N^+$ ,  $NO^+$ ,  $O_2^+$ ,  $N_2^+$ ) and seven neutral species (H, He, O, N, NO, O<sub>2</sub>, N<sub>2</sub>) are used in the model in the numerical experiments of this study.

Neutral temperature and composition are specified by the Mass Spectrometer and Incoherent Scatter radar (MSIS) model (Hedin, 1987), except nitric oxide, which is not included in the MSIS model. A simple expression of the NO density is used (Mitra, 1968; Bailey & Balan, 1996):

$$n[\text{NO}] = 0.4 \exp(-3700/T_n) n[\text{O}_2] + 5 \times 10^{-7} n[\text{O}] \quad [\text{cm}^{-3}].$$

The neutral winds are from the Horizontal Wind Model (HWM) (Hedin et al., 1991). The initial conditions for plasmas are generated from the International Reference Ionosphere (IRI) model (Bilitza, 2018). Fixed  $F10.7 = 181$  and  $A_p = 1$  are used.

As discussed previously, the dynamics, diffusion and physical-chemical forcing are solved sequentially. The time step for diffusion and physics-chemistry is 15 seconds. The time step for the parallel dynamics solver is *adaptive* or sub-time-stepping according to the Courant-Friedrichs-Lewy (CFL) criteria.

The slope limiter is applied to the characteristic variables in the dynamics step and to the primitive variables in the physics-chemistry step. The exponential filter is only used for the ion and electron temperatures in the diffusion step. In all the cases, the smoothness indicator ( $S_I$ ) is used to choose where to applied the limiter or filter; the same  $C_R = 1.0 \times 10^{-6}$  is used in the smoothness threshold; and the same filter order  $s = 6$  is used

**Table 2.** The relative wallclock time for the simulations.

	K101	K135	K201
N2	0.38		1.37
N3	0.62	1.09	
N4	1.00		

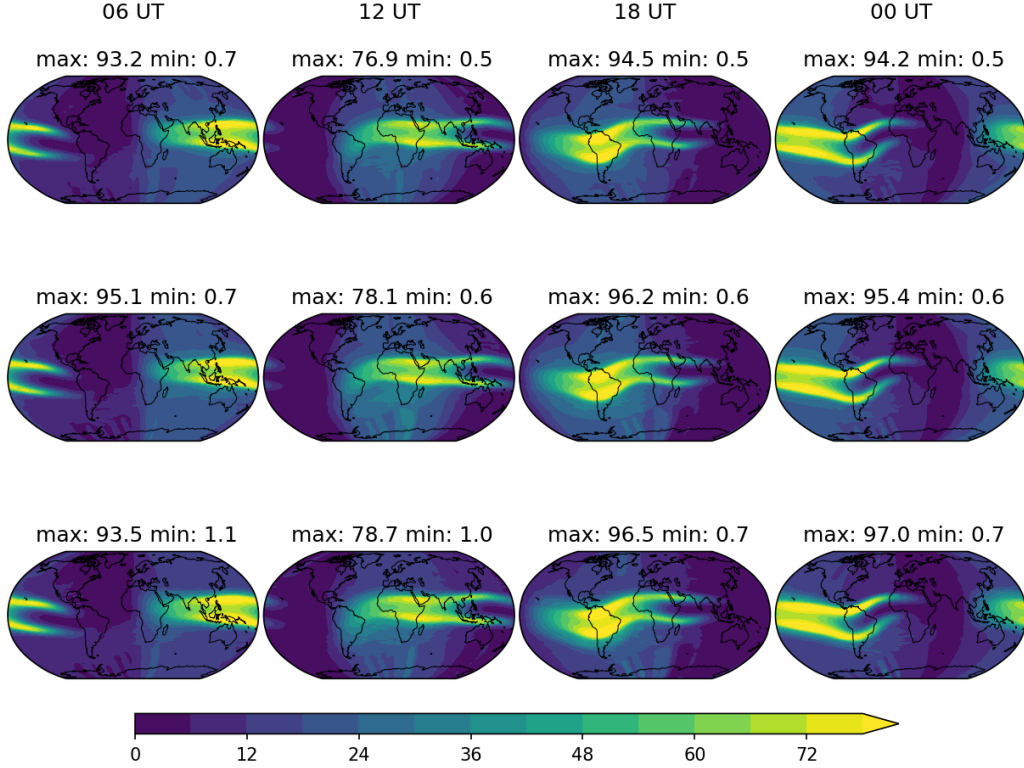


**Figure 1.** The TEC simulations, using the same number of elements (K101), but varying polynomial orders  $N$ : the first row is with  $N2$ , the second row with  $N3$ , and the third row with  $N4$ . Four UT times (06, 12, 18, and 00 UT) are shown, respectively for 6, 12, 18 and 24 hour simulations, initialized at 00 UT on 21 March 2000.

342 in the exponential filter; see Appendix A for details. These parameters, as well as the  
 343 polynomial order  $N$ , are specified at the run time from the Fortran *namelist* input.

344 Table 2 shows the relative run/wall-clock time for each simulation. The run time  
 345 for the second set of simulations (with similar resolutions) show that the higher order  
 346 simulation uses less time.

### 347 3.2 Simulating the total electron content (TEC)

348 We compare the simulations with different combinations of number of elements (K)  
 349 and polynomial orders (N). Figure 1 shows the vertically-integrated TEC from the first  
 350 set of runs which keeps the same number of elements (K101) and varying the poly-  
 351 nomial orders ( $N = 2, 3, 4$ ). Figure 2 shows the vertically-integrated TEC from the sec-  
 352 ond set of runs which varies both the number of elements and the polynomial orders such

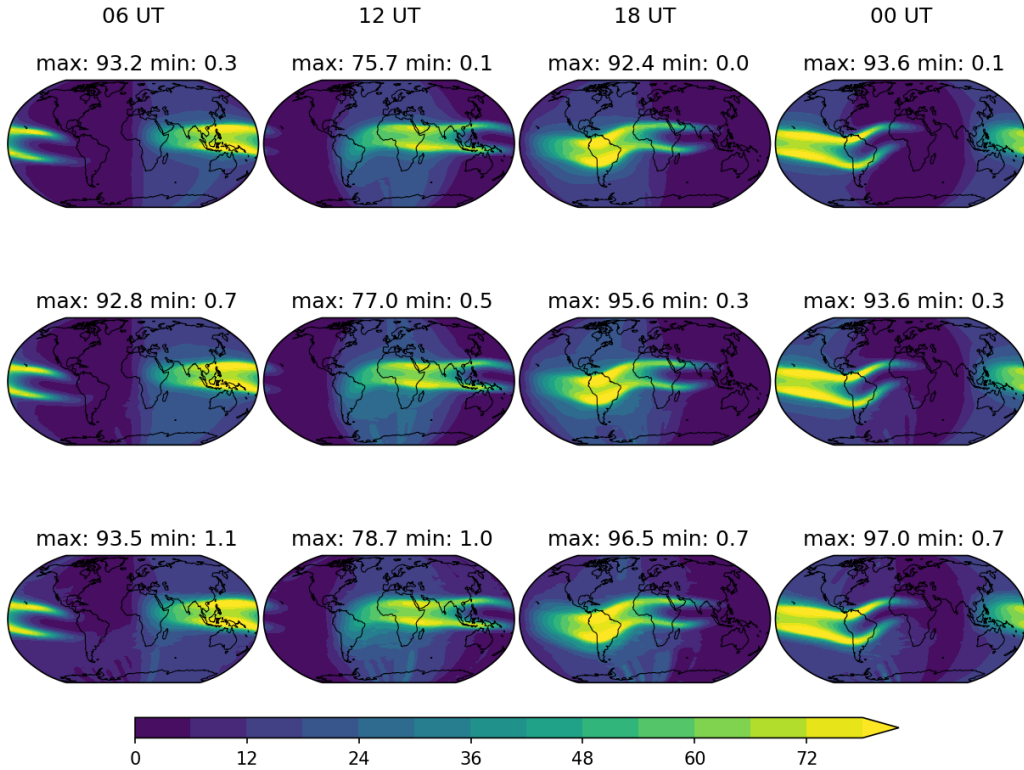


**Figure 2.** The TEC simulations, using varying number of elements  $K$  and varying polynomial orders  $N$ : the first row is with K201 and N2, the second row with K135 and N3, and the third row with K101 and N4. Four UT times (06, 12, 18, and 00 UT) are shown, respectively for 6, 12, 18 and 24 hour simulations, initialized at 00 UT on 21 March 2000.

353 that the overall resolutions are similar. The overall TEC pattern such as the equatorial  
 354 fountain effect (e.g., R. Schunk & Nagy, 2009) and the east-west movement of TEC are  
 355 all well simulated. Comparable TECs are obtained with different K/N combinations; the  
 356 differences of the TEC maxima are less than 5%. The *converging* results of the simula-  
 357 tions using different combinations of K/N indicate the robustness of the algorithms and  
 358 implementation.

359 The maxima of TEC are slightly higher for runs with higher polynomial order, ex-  
 360 cept for simulations with N3 at 06 UT, possibly because the dynamical DG model has  
 361 not yet fully spun up from the cold start initialized from the empirical International Ref-  
 362 erence Ionosphere (IRI) data model. Runs with the higher polynomial order also have  
 363 slightly higher minima values. These results indicate that the higher order of accuracy  
 364 (using higher polynomial order) also imply a higher resolving power (resolutions) for model  
 365 simulations.

### 366 3.3 Capturing the terminator effect

367 An interesting feature of the model is that it can capture very well the termina-  
 368 tor effect, i.e., the distinction between before and after the sunrise. The is clearly shown  
 369 in the  $\text{He}^+$  density field (Fig. 3), most noticeably at 14 UT and 15 UT, or at 2 AM and  
 370 3 AM local time. The production and loss of  $\text{He}^+$  are directly through photoionization  
 371 with the sunrise and chemical loss during the nighttime (e.g., Denton et al., 2002). This

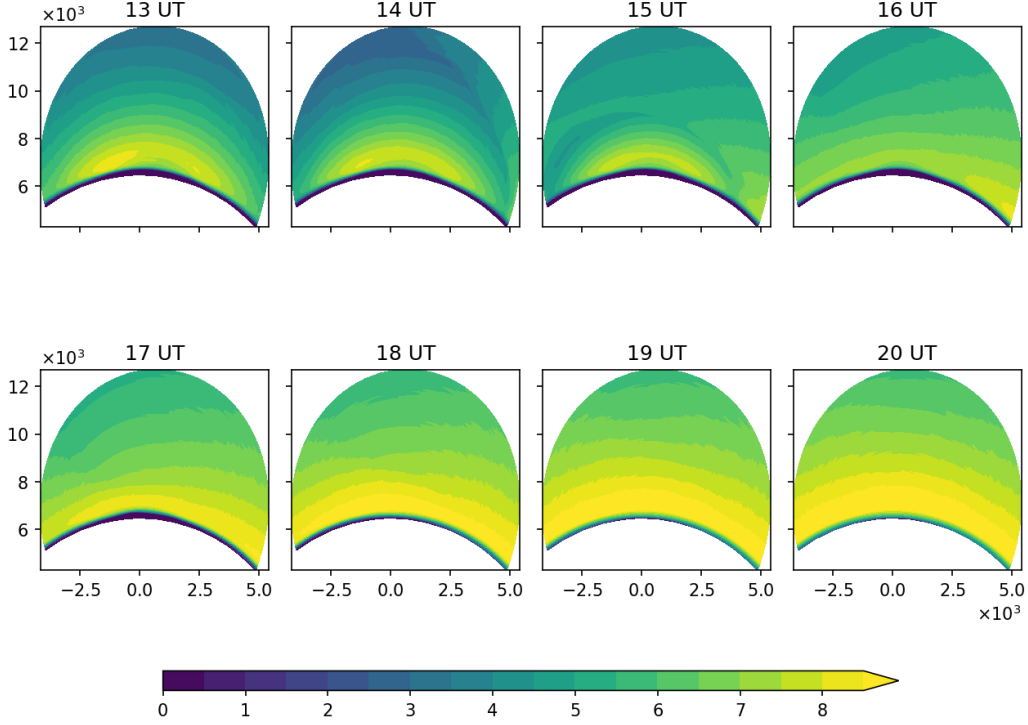


**Figure 3.** The meridional plane plot of the  $\text{He}^+$  density,  $\log_{10} n_{\text{He}^+} [\text{m}^{-3}]$ , at the magnetic longitude  $180^\circ$ , showing the dawn terminator effect. The simulation results from the K101/N2 run are shown every hour from 13 to 20 UT, initialized at 00 UT on 21 March 2000. The geocentric  $x$ - and  $y$ -coordinates in  $[10^3 \text{ km}]$  are used in the plot, with  $x$  from north to south.

372 dawn terminator effect can also potentially affect the formation of the  $\text{He}^+$  layer in ob-  
 373 servations and in modeling (e.g., Wilford et al., 2003).

374 The model’s ability to capture the terminator effect indicates that the effectiveness  
 375 of the model algorithms in capturing the sharp gradients, which is needed in modeling  
 376 small scale phenomena such as ionospheric irregularities.

377 The field-aligned velocity of  $\text{He}^+$  (Fig. 4) shows the significant dynamic response  
 378 of wind to the pressure changes resulting from the ion density changes with the sunrise.  
 379 However, we don not see such large gradient and dramatic changes in the  $\text{He}^+$  ion tem-  
 380 perature field, as they are shown in the density and field-line-aligned velocity fields. This  
 381 may be due to the large thermal diffusivity along the field lines. The terminal effect and  
 382 the response of wind are captured in all other simulations.

#### 383 4 Summary and conclusions

384 In this study, we explore the application of the high-order numerical methods for  
 385 ionosphere-plasmasphere modeling. Specifically, the nodal discontinuous Galerkin (DG)  
 386 method is used to solve the dynamic equations (conservation laws with gravity and dif-  
 387 fusion) along the magnetic field lines. A positive-definite integration scheme, the Patankar-  
 388 Euler scheme, is used to solve the physical-chemical ODEs. A simple ExB drift model  
 389 and semi-Lagrangian transport scheme are used for the perpendicular dynamics. The  
 390 model uses the ragged array of variable length to better handle the varying number of  
 391 points along different field lines. It also uses the MPI-IO for efficient parallel I/O.

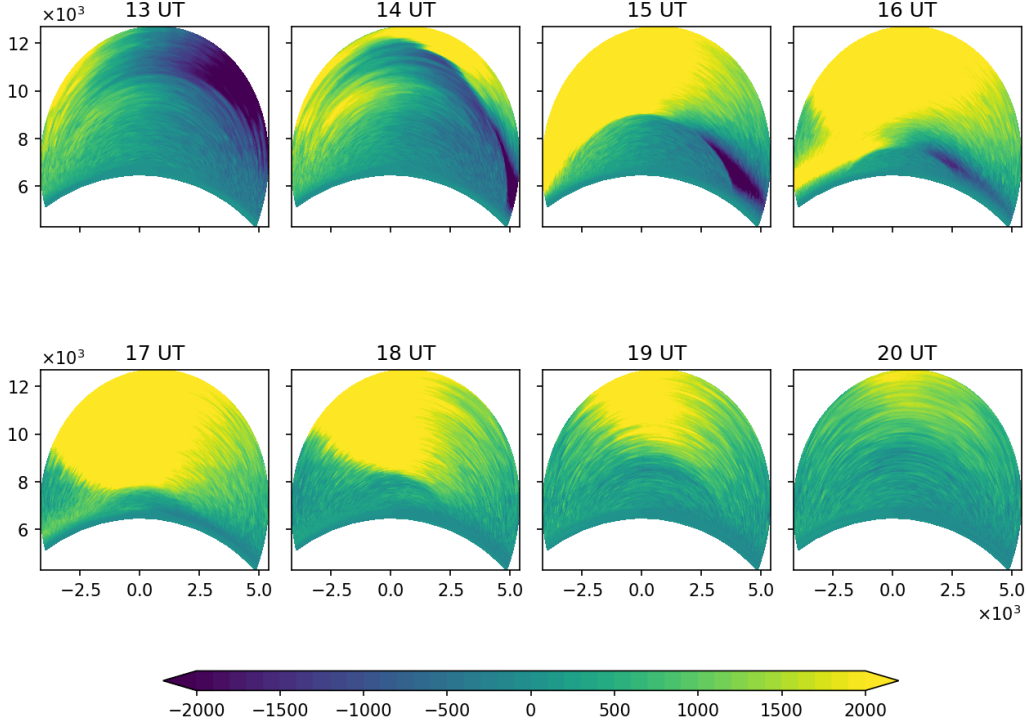


**Figure 4.** The meridional plane plot of the  $\text{He}^+$  velocity [ $\text{m s}^{-1}$ ] along the field line at the magnetic longitude  $180^\circ$ . The simulation results from the K101/N2 run are shown every hour from 13 to 20 UT, initialized at 00 UT on 21 March 2000. The geocentric  $x$ - and  $y$ -coordinates in [ $10^3$  km] are used in the plot, with  $x$  from north to south.

392 The numerical simulations with different combinations of number of elements (K)  
 393 and polynomial orders (N) show remarkable similarity. These *converging* results indicate  
 394 the robustness of the algorithms and their implementation. The model also captures the  
 395 dawn terminator effect very well as shown in the  $\text{He}^+$  density field.

396 There are several areas that need to be explored for application of high-order nu-  
 397 merical methods in ionosphere-plasmasphere modeling. The DG solver for ionospheric  
 398 dynamo equation and conservative high-order transport schemes for ExB drift, such as  
 399 the semi-Lagrangian discontinuous Galerkin (SLDG) scheme, will be the next step.

## 400 Appendix A Limiter, exponential filter and smoothness indicator

401 The choice and application of the limiters or filters are important to the success  
 402 of the high-order DG methods. And the smoothness indicator can be used to decide where  
 403 to apply the limiter or filter.

### 404 A1 The slope limiter

405 Limiter or reconstruction is one of the most important components for any success-  
 406 ful implementation of high-order numerical methods. We discuss one of the limiters, the  
 407 minmod slope limiter. First, define the minmod function

$$408 \quad \text{minmod}(a_1, \dots, a_m) = \begin{cases} s \min_{1 \leq i \leq m} |a_i| & \text{if } |s| = 1, \\ 0 & \text{otherwise,} \end{cases} \quad s = \frac{1}{m} \sum_{i=1}^m \text{sign}(a_i). \quad (\text{A1})$$

409 The minmod function returns the smallest of its arguments if all arguments have the same  
410 sign, otherwise it returns zero. Now define the interface fluxes as

$$411 \quad v_l^k = \bar{u}_h^k - \min\text{mod}(\bar{u}_h^k - u_l^k, \bar{u}_h^k - \bar{u}_h^{k-1}, \bar{u}_h^k - \bar{u}_h^{k+1}),$$

$$412 \quad v_r^k = \bar{u}_h^k + \min\text{mod}(u_r^k - \bar{u}_h^k, \bar{u}_h^k - \bar{u}_h^{k-1}, \bar{u}_h^k - \bar{u}_h^{k+1}),$$

414 where  $\bar{u}_h^k$  is the cell average. Then, the slope limited solution is given by

$$415 \quad \Pi^1 u_h^k(x) = \bar{u}_h^k + (x - x_0^k) \min\text{mod}\left((u_h^k)_x, \frac{\bar{u}_h^k - \bar{u}_h^{k+1}}{h/2}, \frac{\bar{u}_h^k - \bar{u}_h^{k-1}}{h/2}\right),$$

416 where  $x_0^k$  is the center coordinate of  $D^k$ . In this study, the smoothness indicator is used  
417 to decide where to apply the limiter.

## 418 A2 Limiting the characteristic variables

419 When solving the hyperbolic system of conservation laws, more accurate results can  
420 be obtained if limiter is applied to the characteristic variables, instead of the conserva-  
421 tive variables (e.g., Hesthaven, 2018). The characteristic variables can be derived as fol-  
422 lows. The one-dimensional Euler equations can be written in quasilinear form as

$$423 \quad \frac{\partial \mathbf{q}}{\partial t} + \mathcal{A}(\mathbf{q}) \frac{\partial \mathbf{q}}{\partial x} = 0,$$

424 where  $\mathbf{q}$  represents the conservative variables and  $\mathcal{A}(\mathbf{q}) = \nabla_{\mathbf{q}} f$  is the Jacobian of the  
425 flux:

$$426 \quad \mathbf{q} = \begin{bmatrix} \rho \\ \rho u \\ E \end{bmatrix}, \quad \mathcal{A}(\mathbf{q}) = \begin{bmatrix} 0 & 1 & 0 \\ -\frac{3-\gamma}{2}u^2 & (3-\gamma)u & \gamma-1 \\ -\frac{\gamma Eu}{\rho} + (\gamma-1)u^3 & \frac{\gamma E}{\rho} - \frac{3(\gamma-1)u^2}{2} & \gamma u \end{bmatrix}.$$

427 Matrix  $\mathcal{A}$  can be diagonalized as

$$428 \quad \mathbf{S}^{-1} \mathcal{A} \mathbf{S} = \mathbf{\Lambda} = \begin{bmatrix} u+c & 0 & 0 \\ 0 & u & 0 \\ 0 & 0 & u-c \end{bmatrix},$$

429 using

$$430 \quad \mathbf{S} = \begin{bmatrix} \alpha & 1 & \alpha \\ \alpha(u+c) & u & \alpha(u-c) \\ \alpha(H+cu) & \frac{1}{2}u^2 & \alpha(H-cu) \end{bmatrix},$$

431 and

$$432 \quad \mathbf{S}^{-1} = \begin{bmatrix} 2\alpha(\frac{1}{2}(\gamma-1)u^2 - cu) & -2\alpha((\gamma-1)u - c) & 2\alpha(\gamma-1) \\ 1 - \frac{1}{2}(\gamma-1)\frac{u^2}{c^2} & \frac{\gamma-1}{c^2}u & -\frac{\gamma-1}{c^2} \\ 2\alpha(\frac{1}{2}(\gamma-1)u^2 + cu) & -2\alpha((\gamma-1)u + c) & 2\alpha(\gamma-1) \end{bmatrix},$$

433 where we have introduced

$$434 \quad \alpha = \frac{1}{2c}, \quad c = \sqrt{\frac{\gamma p}{\rho}}, \quad H = \frac{E+p}{\rho}$$

435 as a scaling constant, the speed of sound and the enthalpy, respectively.

436 To apply a limiter, the conservative variables  $\mathbf{q}$  are transformed to the character-  
437 istics variables  $\mathbf{R}$  by

$$438 \quad \mathbf{R} = \mathbf{S}^{-1} \mathbf{q},$$

439 to which the limiter is applied. Then the limited characteristic variables  $\tilde{\mathbf{R}}$  are trans-  
440 formed back to the conservative variables  $\tilde{\mathbf{q}}$  by

$$441 \quad \tilde{\mathbf{q}} = \mathbf{S} \tilde{\mathbf{R}},$$

442 which are the model state variables for the next time step. Since this needs to be done  
443 in every time step, it can be expensive to use.

### A3 The exponential filter

The filter matrix of is defined by (e.g., Hesthaven & Warburton, 2008):

$$\mathcal{F} = \mathcal{V}\Lambda\mathcal{V}^{-1},$$

where  $\mathcal{V}$  is the Vandermonde matrix and  $\Lambda$  is a diagonal matrix with entries

$$A_{ii} = \sigma\left(\frac{i-1}{N}\right), \quad i = 1, \dots, N_p,$$

and the exponential filter defined by

$$\sigma(\eta) = \begin{cases} 1, & 0 \leq \eta \leq \eta_c = \frac{N_c}{N}, \\ \exp(-\alpha((\eta - \eta_c)/(1 - \eta_c))^s), & \eta_c < \eta \leq 1. \end{cases}$$

In this study, we choose the cutoff  $N_c = 0$  and the maximum damping parameter  $\alpha = 36$ . The filter order  $s$  is even; increasing  $s$  would reduce filtering.

### A4 The smoothness indicator

The smoothness indicator is defined by (Persson & Peraire, 2006; Ferrero & Larocca, 2016):

$$S_m = \frac{\int_{\mathcal{D}^k} (u_h^k - \tilde{u}_h^k)^2 dx}{\int_{\mathcal{D}^k} (u_h^k)^2 dx},$$

where

$$u_h^k(x, t) = \sum_{i=1}^{N_p} u_h^k(x_i^k, t) \ell_i^k(x), \quad \tilde{u}_h^k(x, t) = \sum_{i=1}^{N_p-1} u_h^k(x_i^k, t) \ell_i^k(x).$$

In practice, the logarithm of the smoothness indicator is used (Ferrero & Larocca, 2016):

$$S_I = \log_{10}(S_m).$$

Expecting  $S_m$  will scale like  $1/N^4$ , the smoothness threshold ( $S_R$ ) of the following form is used:

$$S_R = \log_{10}(C_R/N^4) = \log_{10}(C_R) - 4\log_{10}(N),$$

where  $N = N_p - 1$  is the order of polynomials used in the solutions, thus leaving the constant  $C_R$  as the only parameter to be adjusted according to the problem at hand.

## Appendix B Thermal conductivity and collisional frequency

We summarize computation of thermal conductivity and collisional frequency as used in the SAMI2 model (Huba et al., 2000). Fortran code for computing the physical and chemical forcing terms is extracted from SAMI2 open source code (<https://github.com/NRL-Plasma-Physics-Division/SAMI2>) and modified for the current model.

### B1 Thermal conductivity

The thermal conductivities  $\kappa_i$  and  $\kappa_e$  [eV cm<sup>-1</sup> s<sup>-1</sup> K<sup>-1</sup>] of the  $i$ th ion and electrons are given by (Banks & Kockarts, 1973; Bailey & Balan, 1996)

$$\kappa_i = 4.6 \times 10^4 \frac{n_i T_i^{5/2}}{n_e A_i^{1/2}},$$

where  $A_i$  is the ion mass in [a.m.u.], and

$$\kappa_e = \frac{7.7 \times 10^5 T_e^{5/2}}{1 + 3.22 \times 10^4 T_e^2 N_q / n_e},$$

477 where

$$478 \begin{aligned} N_q &= 1.10 \times 10^{-16} n[\text{O}](1 + 5.7 \times 10^{-4} T_e) + \\ & 2.82 \times 10^{-17} n[\text{N}_2](1 - 1.2 \times 10^{-4} T_e) T_e^{1/2} + \\ & 2.20 \times 10^{-16} n[\text{O}_2](1 + 3.6 \times 10^{-2} T_e^{1/2}). \end{aligned}$$

## 479 **B2 The ion-ion collision frequency**

480 The ion-ion collision frequency  $\nu_{ij}$  in  $[\text{s}^{-1}]$  is given by

$$481 \begin{aligned} \nu_{ij} &= 9.2 \times 10^{-2} n_j \lambda_{ij} \frac{A_j^{1/2}}{A_i} \left(1 + \frac{A_j}{A_i}\right)^{-1/2} \frac{1}{T^{3/2}}, \\ \lambda_{ij} &= 23 - \ln \left[ \frac{A_i + A_j}{A_i T_j + A_j T_i} \left( \frac{n_i}{T_i} + \frac{n_j}{T_j} \right)^{1/2} \right]. \end{aligned}$$

482 where  $A_i$  and  $A_j$  are the atomic ion mass in [a.m.u.],  $T$  is in [eV], and  $n_j$  in  $[\text{cm}^{-3}]$ . Tem-  
483 perature is converted from [K] to [eV] by

$$484 T_{eV} = 8.6174 \times 10^{-5} T_K.$$

## 487 **B3 The ion-neutral collision frequency**

488 The ion-neutral collision frequency  $\nu_{in}$  in  $[\text{s}^{-1}]$  is given by

$$489 \begin{aligned} \nu_{in} &= \frac{m+n}{m_i+m_n} \bar{\nu}_{in}, & (B1) \\ \bar{\nu}_{in} &= 2.69 \times 10^{-9} \frac{\alpha_0 n_n}{\mu_A^{1/2}}, \\ \mu_A &= \frac{A_i A_n}{A_i + A_n}, \end{aligned}$$

491 where  $\alpha_0$  is the polarizability. Several temperature-dependent ion-neutral collision fre-  
492 quencies (Bailey & Balan, 1996) are used in place of (B1):

$$493 \begin{aligned} \nu_{\text{H}^+\text{O}} &= 6.61 \times 10^{-11} n[\text{O}] T^{1/2} (1.00 - 0.047 \log_{10} T)^2, & T = T_{\text{H}^+}, \\ \nu_{\text{O}^+\text{O}} &= 4.45 \times 10^{-11} n[\text{O}] T^{1/2} (1.04 - 0.067 \log_{10} T)^2, & T = (T_{\text{O}^+} + T_n)/2, \\ \nu_{\text{O}_2^+\text{O}_2} &= 2.59 \times 10^{-11} n[\text{O}_2] T^{1/2} (1.00 - 0.073 \log_{10} T)^2, & T = (T_{\text{O}_2^+} + T_n)/2, \\ \nu_{\text{N}_2^+\text{N}_2} &= 5.14 \times 10^{-11} n[\text{N}_2] T^{1/2} (1.00 - 0.069 \log_{10} T)^2, & T = (T_{\text{N}_2^+} + T_n)/2, \end{aligned}$$

494 where the temperature is in [K] and the number density of the neutrals is in  $[\text{cm}^{-3}]$ .

## 501 **B4 The electron-neutral collisional heating**

502 The electron-neutral heating term (7d) can be written as

$$503 \begin{aligned} Q_{en} &= \frac{2}{3} \sum_q \frac{m_e m_q}{(m_e + m_q)^2} \nu_{eq} [3(T_q - T_e)], \\ &= \frac{2}{3} \sum_q \bar{\nu}_{eq} (T_q - T_e), \end{aligned}$$

504 where  $\bar{\nu}_{eq}$  denotes the effective heating rate. The elastic electron-neutral collisional heat-  
505 ing rates are given by (Banks & Kockarts, 1973):

$$506 \begin{aligned} \bar{\nu}_{e\text{N}_2} &= 1.2 \times 10^{-19} n[\text{N}_2](1 - 1.2 \times 10^{-4} T_e) T_e, \\ \bar{\nu}_{e\text{O}_2} &= 7.9 \times 10^{-19} n[\text{O}_2](1 - 3.6 \times 10^{-2} T_e^{1/2}) T_e^{1/2}, \\ \bar{\nu}_{e\text{O}} &= 7.2 \times 10^{-18} n[\text{O}] T_e^{1/2}, \\ \bar{\nu}_{e\text{H}} &= 6.3 \times 10^{-16} n[\text{H}](1 - 1.35 \times 10^{-4} T_e) T_e^{1/2}. \end{aligned}$$

508

511 The units are collisional heating rates [ $\text{eV K}^{-1} \text{s}^{-1}$ ], the temperature [K] and the num-  
512 ber density [ $\text{cm}^{-3}$ ].

## 513 B5 The photoelectron heating

514 At altitudes lower than 300 km, the photoelectron heating rate [ $\text{eV s}^{-1}$ ] is computed  
515 from

$$516 \quad Q_{\text{phe}} = \frac{2}{3} \frac{1}{n_e} \epsilon P_{\text{photo}},$$

$$517 \quad \epsilon = \exp[-p(x)],$$

$$518 \quad p(x) = 12.75 + 6.94x + 1.66x^2 + 0.08034x^3 + 0.001996x^4,$$

$$519 \quad x = \ln\left(\frac{n_e}{n[\text{O}_2] + n[\text{N}_2] + 0.1n[\text{O}]}\right),$$

521 where  $P_{\text{photo}}$  is the total photoionization rate. At altitudes higher than 300 km, the pho-  
522 toelectron heating rate is computed as

$$523 \quad Q_{\text{phe}}(\ell) = \frac{2}{3} \frac{B(\ell)}{B(\ell_{300})} Q_{\text{phe}}(\ell_{300}) \exp\left(-C_{qe} \int_{\ell_{300}}^{\ell} n_e d\ell\right),$$

524 where  $B$  is the magnetic field strength, the constant  $C_{qe}$  is taken to be  $7.0 \times 10^{-14} \text{ cm}^2$ ,  
525 and the integration along the flux tube is from both hemispheres.

## 526 References

- 527 Anderson, E., Bai, Z., Bischof, C., Blackford, S., Demmel, J., Dongarra, J., ...  
528 Sorensen, D. (1999). *LAPACK Users' Guide* (Third ed.). Philadelphia, PA:  
529 Society for Industrial and Applied Mathematics.
- 530 Bailey, G. J., & Balan, N. (1996). A low-latitude ionosphere-plasmasphere model. In  
531 R. W. Schunk (Ed.), *Handb. ionos. model.* (pp. 173–206).
- 532 Banks, P. M., & Kockarts, G. (1973). *Aeronomy, Part B*. New York: Elsevier. doi:  
533 10.1016/C2013-0-10329-7
- 534 Bilitza, D. (2018). IRI the international standard for the ionosphere. *Adv. Radio*  
535 *Sci.*, *16*, 1–11. doi: 10.5194/ars-16-1-2018
- 536 Burchard, H., Deleersnijder, E., & Meister, A. (2003). A high-order conservative  
537 Patankar-type discretisation for stiff systems of production-destruction equations.  
538 *Appl. Numer. Math.*, *47*(1), 1–30. doi: 10.1016/S0168-9274(03)00101-6
- 539 Cai, X., Guo, W., & Qiu, J.-M. (2017). A high order conservative semi-Lagrangian  
540 discontinuous Galerkin method for two-dimensional transport simulations. *J. Sci.*  
541 *Comput.*, *73*(2-3), 514–542. doi: 10.1007/s10915-017-0554-0
- 542 Canuto, C., Hussaini, M. Y., Quarteroni, A., & Zang, T. A. (2006). *Spectral Meth-*  
543 *ods: Fundamentals in Single Domains*. Berlin, Heidelberg: Springer Berlin Heidel-  
544 berg. doi: 10.1007/978-3-540-30726-6
- 545 Cockburn, B., Karniadakis, G. E., & Shu, C.-W. (2000). The Development of Dis-  
546 continuous Galerkin Methods. In B. Cockburn, G. E. Karniadakis, & C.-W. Shu  
547 (Eds.), *Discontinuous galerkin methods* (pp. 3–50). Springer, Berlin, Heidelberg.  
548 doi: 10.1007/978-3-642-59721-3\_1
- 549 Courant, R., Friedrichs, K., & Lewy, H. (1967). On the partial difference equations  
550 of mathematical physics. *IBM J. Res. Dev.*, *11*(2), 215–234. doi: 10.1147/rd.112  
551 .0215
- 552 Denton, M. H., Bailey, G. J., Wilford, C. R., Rodger, A. S., & Venkatraman,  
553 S. (2002).  $\text{He}^+$  dominance in the plasmasphere during geomagnetically dis-  
554 turbed periods: 1. Observational results. *Ann. Geophys.*, *20*(4), 461–470. doi:  
555 10.5194/angeo-20-461-2002

- 556 Deville, M. O., Fischer, P. F., & Mund, E. H. (2002). *High-Order Methods*  
 557 *for Incompressible Fluid Flow*. Cambridge University Press. doi: 10.1017/  
 558 cbo9780511546792
- 559 Fazio, R., & Jannelli, A. (2010). Second order numerical operator splitting for 3D  
 560 advection–diffusion–reaction models. In *Numer. math. adv. appl. 2009* (pp. 317–  
 561 324). Berlin, Heidelberg: Springer Berlin Heidelberg. doi: 10.1007/978-3-642-11795  
 562 -4\_33
- 563 Fejer, B. G., Souza, J. R., Santos, A. S., & Costa Pereira, A. E. (2005). Clima-  
 564 tology of F region zonal plasma drifts over Jicamarca. *J. Geophys. Res. Sp. Phys.*,  
 565 110(A12), 12310. doi: 10.1029/2005JA011324
- 566 Ferrero, A., & Larocca, F. (2016). Feedback filtering in discontinuous Galerkin  
 567 methods for Euler equations. *Prog. Comput. Fluid Dyn. An Int. J.*, 16(1), 14. doi:  
 568 10.1504/PCFD.2016.074221
- 569 Giraldo, F., & Restelli, M. (2008). A study of spectral element and discontinuous  
 570 Galerkin methods for the Navier–Stokes equations in nonhydrostatic mesoscale  
 571 atmospheric modeling: Equation sets and test cases. *J. Comput. Phys.*, 227(8),  
 572 3849–3877. doi: 10.1016/j.jcp.2007.12.009
- 573 Gottlieb, S., Shu, C. W., & Tadmor, E. (2001). Strong stability-preserving high-  
 574 order time discretization methods. *SIAM Rev.*, 43(1), 89–112. doi: 10.1137/  
 575 S003614450036757X
- 576 Gropp, W., Hoefler, T., Thakur, R., & Lusk, E. (2014). *Using Advanced MPI: Mod-  
 577 ern Features of the Message-Passing Interface*. The MIT Press.
- 578 Gustafsson, B. (2008). *High Order Difference Methods for Time Dependent PDE*  
 579 (Vol. 38). Berlin, Heidelberg: Springer Berlin Heidelberg. doi: 10.1007/978-3-540  
 580 -74993-6
- 581 Hain, K. H. (1987). The partial donor cell method. *J. Comput. Phys.*, 73(1), 131–  
 582 147. doi: 10.1016/0021-9991(87)90110-0
- 583 Hedin, A. E. (1987). MSIS-86 thermospheric model. *J. Geophys. Res.*, 92(A5), 4649.  
 584 doi: 10.1029/ja092ia05p04649
- 585 Hedin, A. E., Biondi, M. A., Burnside, R. G., Hernandez, G., Johnson, R. M.,  
 586 Killeen, T. L., ... Virdi, T. S. (1991). Revised global model of thermosphere  
 587 winds using satellite and ground-based observations. *J. Geophys. Res.*, 96(A5),  
 588 7657. doi: 10.1029/91ja00251
- 589 Hesthaven, J. S. (2018). *Numerical Methods for Conservation Laws: From Analysis*  
 590 *to Algorithms*. Philadelphia, PA: Society for Industrial and Applied Mathematics.  
 591 doi: 10.1137/1.9781611975109
- 592 Hesthaven, J. S., & Warburton, T. (2008). *Nodal Discontinuous Galerkin Methods*  
 593 (Vol. 54). New York, NY: Springer New York. doi: 10.1007/978-0-387-72067-8
- 594 Huba, J. D. (2003). Hall Magnetohydrodynamics - A Tutorial. In *Sp. plasma simul.*  
 595 (pp. 166–192). Berlin, Heidelberg: Springer Berlin Heidelberg. doi: 10.1007/3-540  
 596 -36530-3\_9
- 597 Huba, J. D., Joyce, G., & Fedder, J. A. (2000). Sami2 is Another Model of the Iono-  
 598 sphere (SAMI2): A new low-latitude ionosphere model. *J. Geophys. Res.*, 105.
- 599 Huba, J. D., & Liu, H. L. (2020). Global Modeling of Equatorial Spread F with  
 600 SAMI3/WACCM-X. *Geophys. Res. Lett.*, 47(14). doi: 10.1029/2020GL088258
- 601 Mitra, A. P. (1968). A review of D-region processes in non-polar latitudes. *J. Atmos.*  
 602 *Terr. Phys.*, 30(6), 1065–1114. doi: 10.1016/S0021-9169(68)90606-5
- 603 Patankar, S. V. (1980). *Numerical Heat Transfer and Fluid Flow*. CRC Press. doi:  
 604 10.1201/9781482234213
- 605 Persson, P. O., & Peraire, J. (2006). Sub-cell shock capturing for discontinuous  
 606 Galerkin methods. In *44th aiaa aerosp. sci. meet.* (Vol. 2, pp. 1408–1420). doi: 10  
 607 .2514/6.2006-112
- 608 Proft, J., & Rivière, B. (2009). Discontinuous Galerkin methods for convection-  
 609 diffusion equations for varying and vanishing diffusivity. *Int. J. Numer. Anal.*

- 610 *Model.*, 6(4), 533–561.
- 611 Scherliess, L., & Fejer, B. (1999). Radar and satellite global equatorial F region ver-  
612 tical model. *J. Geophys. Res.*, 104, 6829–6842.
- 613 Schunk, R., & Nagy, A. (2009). *Ionospheres: Physics, Plasma Physics, and Chem-*  
614 *istry* (2nd ed.). Cambridge University Press. doi: 10.1017/CBO9780511635342
- 615 Schunk, R. W. (Ed.). (1996). *Handbook of Ionospheric Models*. SCOSTEP. Re-  
616 trieved from [https://www.bc.edu/content/dam/bc1/offices/ISR/SCOSTEP/](https://www.bc.edu/content/dam/bc1/offices/ISR/SCOSTEP/Multimedia/other/ionospheric-models.pdf)  
617 [Multimedia/other/ionospheric-models.pdf](https://www.bc.edu/content/dam/bc1/offices/ISR/SCOSTEP/Multimedia/other/ionospheric-models.pdf)
- 618 Shahbazi, K. (2005). An explicit expression for the penalty parameter of the inte-  
619 rior penalty method. *J. Comput. Phys.*, 205(2), 401–407. doi: 10.1016/j.jcp.2004  
620 .11.017
- 621 Strang, G. (1968). On the Construction and Comparison of Difference Schemes.  
622 *SIAM J. Numer. Anal.*, 5(3), 506–517. doi: 10.1137/0705041
- 623 Wang, H. (2021). A general curvilinear magnetic field-line-following coordinate sys-  
624 tem for ionosphere-plasmasphere modeling. *Earth Sp. Sci. Open Arch.*, 13. doi: 10  
625 .1002/essoar.10508238.1
- 626 Wilford, C. R., Moffett, R. J., Rees, J. M., Bailey, G. J., & Gonzalez, S. A. (2003).  
627 Comparison of the He+ layer observed over Arecibo during solar maximum and  
628 solar minimum with CTIP model results. *J. Geophys. Res. Sp. Phys.*, 108(A12),  
629 1452. doi: 10.1029/2003JA009940
- 630 Zettergren, M., & Semeter, J. (2012). Ionospheric plasma transport and loss in auro-  
631 ral downward current regions. *J. Geophys. Res.*, 117(A6), A06306. doi: 10.1029/  
632 2012JA017637